



A portable microfluidic chip device integrated with a real-time CTCs detection model for point-of-care testing of early-stage lung cancer

Asyidicky Firmanto ^a, Tsung-Wei Lin ^a, Yi-Chun Du ^{a,b,*}, Chun-Ping Jen ^{c,d}

^a Department of Biomedical Engineering, National Cheng Kung University, Tainan 70105, Taiwan

^b Medical Device Innovation Center, National Cheng Kung University, Tainan 70105, Taiwan

^c Department of Mechanical Engineering and Advanced Institute of Manufacturing for High-Tech Innovations, National Chung Cheng University, Chia-Yi 62102, Taiwan

^d School of Dentistry, College of Dental Medicine, Kaohsiung Medical University, Kaohsiung 80708, Taiwan



ARTICLE INFO

Keywords:

Lung cancer
Microfluidic chip
YOLOv8
Point of care testing

ABSTRACT

Lung cancer remains the leading cause of cancer-related deaths globally. Despite advances in diagnostic technologies, they are mostly reliant on laboratories in medical institutions and utilizing invasive methods, which present challenges in early-stage lung cancer detection. Although some research focused on automation and developing microfluidic-chip-based application for circulating tumor cells (CTCs) analysis based on liquid biopsy sampling, most of these approaches focus on static image analysis of CTCs, which leads to an inability to maintain target detection accuracy in dynamic fluid environments. This study introduced an improved real-time detection model of magnetic-bead-attached CTCs based on the fundamental YOLOv8 model. The proposed model was trained and evaluated on a microfluidic chip-based dynamic fluid platform composed of modules proposed in previous studies. Moreover, to improve the Point-of-Care Testing (POCT) implementation for early-stage lung cancer detection, this study also integrated a semi-automatic microfluidic platform and imaging flow cytometry (IFC) with the improved real-time CTCs detection model, resulting in the development of a portable device accompanied by the performance evaluations. According to the experimental results, the proposed improved YOLOv8 model achieved higher performance than fundamental YOLOv8 model. Additionally, this study compared the counted result from the portable device to the ground truth that was counted by the attendants, which achieved a robust counting accuracy (over 90%). This demonstrates the proposed method has high potential to assist in reducing labor-intensive tasks, further improving POCT implementation for early-stage lung cancer detection.

1. Introduction

Lung cancer remains the leading cause of cancer-related deaths worldwide, accounting for approximately 1.8 million deaths annually [1–4]. Despite advancements in treatment, lung cancer is often diagnosed at a late stage, leading to limited treatment options and poor survival rates [5,6]. Therefore, early-stage detection of lung cancer is crucial in improving outcomes, allowing for timely interventions that can significantly reduce mortality rates. However, existing clinical diagnostic methods are often invasive, require sophisticated laboratory setups, and are unsuitable for repeated diagnoses due to the physiological burden they impose [7,8]. These limitations present significant challenges in early-stage lung cancer detection and the implementation of Point-of-Care Testing (POCT). To address these challenges, liquid

biopsy has emerged as a promising approach for early-stage cancer detection and POCT applications [9–11]. Circulating tumor cells (CTCs), which are cells shed from primary tumors and enter the circulatory system, have been widely used as a diagnostic standard for early-stage lung cancer [12–14]. To isolate CTCs, magnetic beads functionalized with antibodies that bind to CTC surface biomarkers have been employed [15,16]. However, current methods for analyzing CTCs rely on manual counting and cytometry techniques, which are labor-intensive and require specific instruments in professional laboratories, making them unsuitable for POCT applications [17–20].

Recent advancements in microfluidic technologies and object detection models have shown potential for improving CTC analysis. For instance, prior studies have explored the use of magnetic beads functionalized with antibodies to capture and isolate CTCs from blood

* Corresponding author at: Department of Biomedical Engineering, National Cheng Kung University, Tainan 70105, Taiwan.

E-mail address: terrydu@gs.ncku.edu.tw (Y.-C. Du).

samples [19,20]. While this approach demonstrated significant potential, it still relies on cytometry instruments that require sophisticated laboratory setups, limiting its portability and automation for POCT implementation. To reduce laboratory setup and hardware requirements, imaging flow cytometry (IFC) has emerged as a promising technology. IFC acquires single-cell images at high throughput using minimal hardware, such as a microscope and CMOS camera. Heo et al. [21,22] developed a real-time moving object detector for label-free IFC, achieving fast and reliable accuracy under high cell throughput. However, the label-free nature of this approach complicates the imaging process, reducing the robustness of specific object detection. To enhance the robustness of CTC detection for early-stage cancer diagnosis, Ruiz-Rodríguez, A.J. et al. [23,24] proposed combining commercialized microfluidic isolation platforms with IFC instruments. This approach achieved a combined CTC recovery rate of over 70 % and improved detection robustness. However, the commercialized instruments used in this approach lack portability and automation, making them unsuitable for POCT implementation.

Building on these advancements, this study focuses on developing a real-time detection model capable of accurately identifying and counting CTCs in dynamic fluid environments, leveraging the YOLOv8 model and a microfluidic chip-based platform to address the limitations of current static imaging methods. By integrating dynamic fluid analysis - with advanced object detection techniques, we aim to provide a portable, automated solution that enhances the practicality and accuracy of POCT for early-stage lung cancer diagnosis. Specifically, this study addresses two primary requirements for early-stage lung cancer detection and POCT implementation: (1) an improved object detection method for analyzing cell-binding magnetic beads under dynamic fluid conditions, and (2) a portable device integrating a dynamic fluid platform and an embedded computing unit with the improved object detection method. To achieve this, we propose an improved real-time detection model based on YOLOv8 for detecting magnetic-bead-attached CTCs. This model is trained and evaluated on a microfluidic chip-based dynamic fluid platform, which was developed based on modules proposed in previous studies [27,28]. Furthermore, we integrate a semi-automatic microfluidic platform and IFC with the improved YOLOv8 model to develop a portable device. This device enhances the robustness of CTC detection and supports POCT implementation for early-stage lung cancer detection.

2. Material and methods

In this study, we proposed the real-time detection model of magnetic-bead-attached CTCs that maintained robust accuracy under dynamic fluid environment. Additionally, we developed a portable device which integrated the components of microfluid chip based dynamic fluid platform with embedded computing unit for the proposed method. To illustrate the evaluation platform for the proposed method, this study first introduces the microfluidic-chip-based dynamic fluid platform, which was utilized to collect image datasets for training and evaluating the proposed method.

2.1. Microfluidic chip based dynamic fluid platform

In this study, we developed a microfluidic-chip-based dynamic fluid platform based on our previous research [19,20], to improve and evaluate the proposed real-time detection model of magnetic-bead-attached CTCs. This platform can be introduced by dividing into three parts: (1) Liquid biopsy sample preparation; (2) Microfluidic chip configuration; (3) Dynamic fluid platform setup. The microfluidic chip-based dynamic fluid platform was optimized to maintain a consistent flow rate of 10 $\mu\text{L}/\text{min}$, ensuring that the detection process accurately reflects the dynamic nature of blood circulation. This setup allows for real-time monitoring of CTCs and magnetic beads as they interact within the microfluidic channels, providing a robust evaluation of the proposed detection

model. Prior to sample preparation, the A549 and HeLa cell lines used in this study were procured from MdBio, Inc. (Taipei City, Taiwan). A549 cells were cultured in Dulbecco's Modified Eagle Medium (DMEM), while HeLa cells were maintained in Eagle's Minimum Essential Medium (EMEM), both supplemented with 10 % fetal bovine serum (FBS), 1 % penicillin-streptomycin, and 3.7 g/L sodium bicarbonate (NaHCO₃), under standard conditions at 37 °C in a humidified atmosphere containing 5 % CO₂. The culture medium was refreshed every 1–2 days, and cells were harvested using 0.25 % trypsin-EDTA, followed by neutralization with FBS-containing medium. Starting with the liquid biopsy sample preparation, clinical blood samples were obtained from patients diagnosed with early-stage lung cancer through an IRB-approved clinical trial at Changhua Christian Hospital, Taiwan (IRB no. 240135IRB). The blood was collected in EDTA tubes, centrifuged at 1,500 rpm for 10 min to separate plasma (which was discarded), and then subjected to red blood cell lysis using ACK lysis buffer for 5 min. The remaining nucleated cell pellet was washed and resuspended in PBS for further analysis. In this study, the acquired sample was divided into an experimental group and a control group. Both the groups were added HeLa cells, which was used to serve as non-lung cancer controls [25]; subsequently, due to the rarity of CTCs, this study utilized A549 cancer cell line to simulate CTCs and was added into the sample of experimental group. Secondly, this study employed a functionalized magnetic bead-based method on the separation of A549 cell. In this method, magnetic beads (4.5 μm in diameter) were functionalized with epithelial cell adhesion molecule (EpCAM) specific DNA aptamers, via a two-step chemical conjugation process using 1-ethyl-3-(3-dimethylaminopropyl) carbodiimide (EDC) and N-hydroxysuccinimide (NHS). Functionalized magnetic beads can bind to the surface biomarkers of A549 cell, thereby aligning to the direction of magnetic field on microfluidic chip; the functionalized magnetic beads were added in both experimental and control group. To minimize interference from non-target components such as white blood cells and red blood cells, the samples underwent a preprocessing step involving red blood cell lysis and density gradient centrifugation, which has been shown to remove up to 95 % of non-target cells. In this study, these preprocessing steps were performed manually using benchtop procedures prior to sample injection into the microfluidic chip and were not integrated into the portable detection system. The purpose of applying these steps was to optimize input sample quality for evaluating the detection model's performance under controlled conditions. Additionally, the specificity of the EpCAM-functionalized magnetic beads ensures selective capture of CTCs, as confirmed by flow cytometry analysis showing less than 5 % binding to non-target cells.

In the second part, the microfluidic chip utilized in this study was based on Serpentine Microchannel with Cavities (SMAC) structure proposed in our previous study [20]; the illustration of microfluidic chip configuration is depicted in Fig. 1. This structure is not only optimized for increasing the interaction surface, but also prolonged the interaction time and capturing efficiency of target cells. To establish a magnetic field on the microfluidic chip, a 0.5 T permanent magnet was embedded in microfluidic chip, placed 3.0 mm from the SMAC structure. This positioning of the magnet was able to enhance the precise bead-CTCs interaction. Moreover, to optimize the interactions, the flow rate of the microfluidic chip was maintained at 10 $\mu\text{L}/\text{min}$, which can minimize turbulence and allow consistent imaging. The coupling efficiency of magnetic beads functionalized with antibody-specific DNA aptamers was determined using a spectrophotometric assay, as previously described [19,20]. The binding ability of the functionalized beads to A549 cells was evaluated by flow cytometry, showing a capture efficiency of 88.4 % under optimal conditions.

The third part of the system involves the setup of the dynamic fluid platform, as illustrated in Fig. 2. Initially, the prepared sample was introduced using a syringe pump system (Model KDS 101, KD Scientific Inc., USA), which controlled the flow rate of the sample from the syringe to the microfluidic chip inlet. Once the sample began circulating

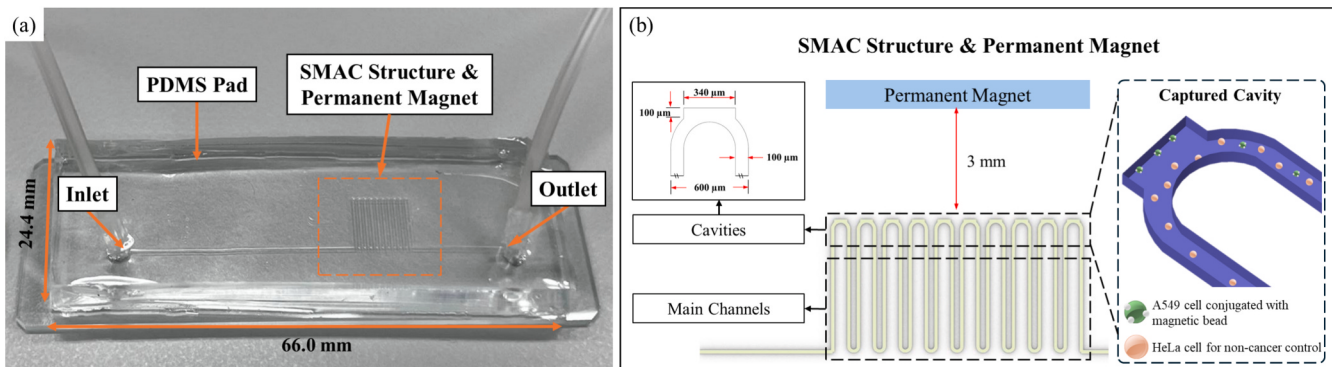


Fig. 1. (a) SMAC structure based microfluidic chip. (b) Illustration for SMAC structure and permanent magnet.

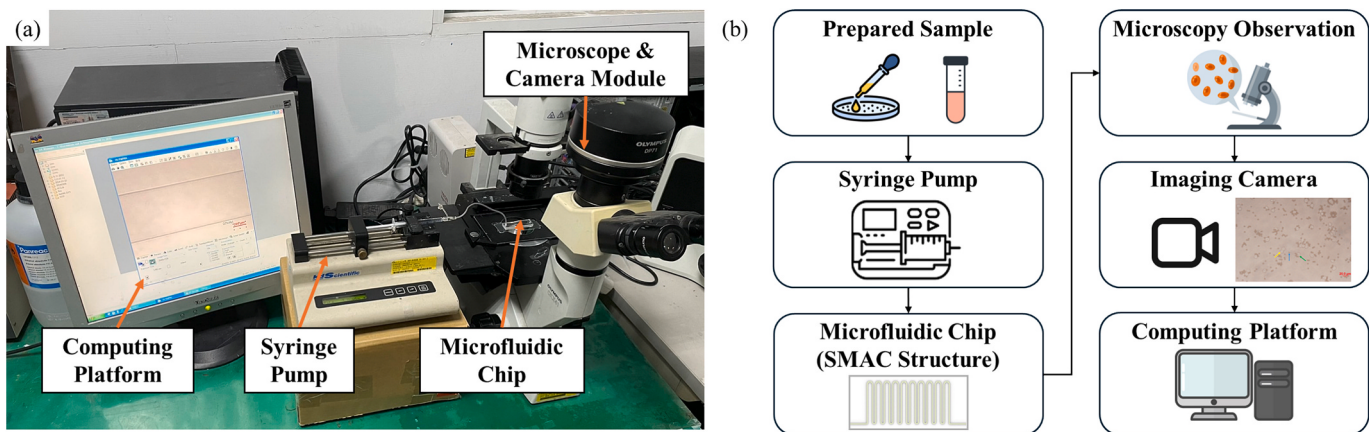


Fig. 2. (a) Configuration of microfluidic chip based dynamic fluid platform. (b) Overall workflow of CTCs analysis based on dynamic fluid platform.

through the microfluidic chip, A549 cells bound to functionalized magnetic beads were isolated in the SMAC structure, due to the magnetic field generated by the permanent magnet embedded in the chip. Following isolation in the SMAC structure, images were captured using a

microscope (CKX41, Olympus, Tokyo, Japan) equipped with a camera (DP71, Olympus, Tokyo, Japan) at a resolution of 2430 x 1260 pixels.

After introducing the evaluation platform for the proposed method, we subsequently illustrate the developed portable device that integrates

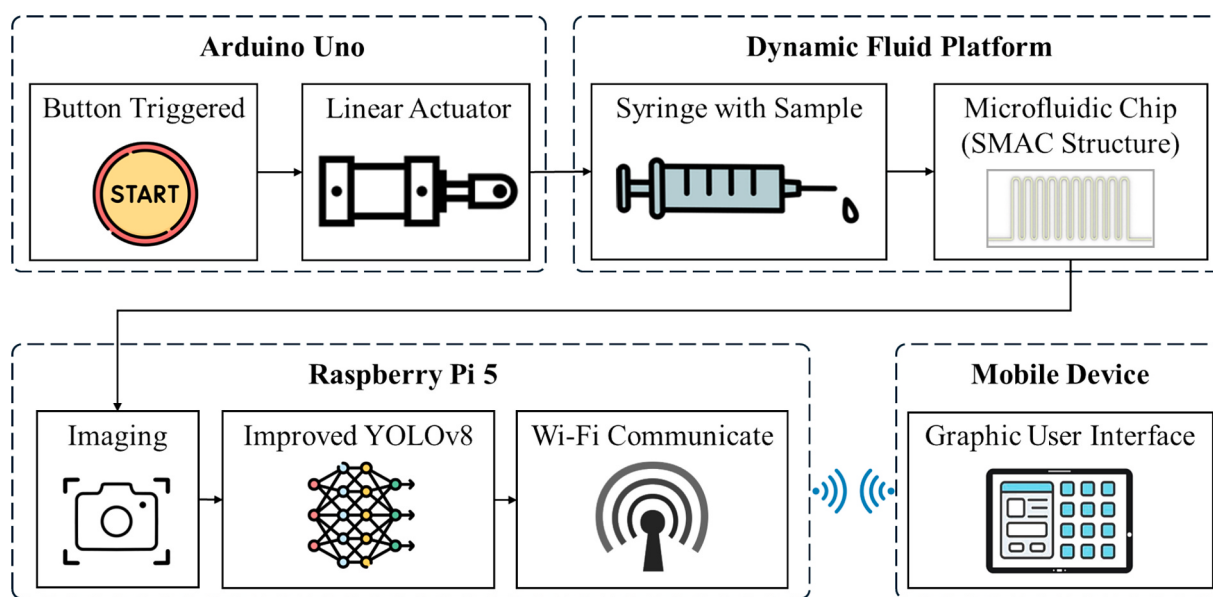


Fig. 3. Overall workflow of a portable device involves a button module activating a servo motor-driven linear actuator to control sample flow from a syringe into a microfluidic chip, followed by image capture with a microscopy-equipped camera; the images are processed by improved YOLOv8 model in real-time and results displayed on a GUI via wireless communication.

components of microfluidic-chip-based dynamic fluid platform with embedded computing unit for the proposed method. Finally, we detail the detection model of magnetic-bead-attached CTCs implemented in the proposed system.

2.2. Portable device integrated dynamic fluid platform and embedded computing unit

To improve the POCT implementation of early-stage lung cancer detection, this study proposed portable device which integrated microfluidic-chip-based dynamic fluid platform and embedded the detection model of magnetic-bead-attached CTCs. The overall workflow of the portable device is illustrated in Fig. 3. In the first step, portable device was triggered by the button module, which subsequently triggers the servo motor-based linear actuator. In the second step, the flow rate of the sample from syringe was controlled by the linear actuator, injecting it into the microfluidic chip. In the third step, the camera module, equipped with a microscopy lens, captures images from the microfluidic chip, which are then processed by the improved YOLOv8 model embedded in the Raspberry Pi 5. Finally, this device uploaded the detection result on the graphic user interface (GUI) through wireless communication.

In Fig. 4(a), the hardware configuration can be divided into electronic and fluidic components. In the fluidic part, this study had built a servo motor based linear actuator to control the flow of samples at a precise rate of 10 $\mu\text{L}/\text{min}$. The flow of samples was injected into the microfluidic chip proposed in this study, lastly output to an acrylic water tank, with the size of 6.5 cm x 6.5 cm x 6 cm. After the sample entered the SMAC structure on microfluidic chip, the A549 cells conjugated with magnetic beads were captured in cavities of SMAC structure. The camera with 40x microscopy lens can capture the image of cavities of SMAC structure on microfluidic chips for subsequent image processing. In the electronic part, this study applied two microcontrollers to achieve higher efficiency of embedded computing unit. The first microcontroller is Arduino Uno, which responsible for controlling SG-90 servo motor module (Tower Pro Pte Ltd., Singapore) and KEYES 3-Colour RGB LED light source module (KEYES Corporation, China); additionally, this microcontroller also received the signal of KEYES brick button module (KEYES Corporation, China) and showed the operation situation on 16 x 2 LCD display module (Displaytech Ltd., Hong Kong). The second microcontroller is Raspberry Pi Model 5, which is responsible for Raspberry Pi Camera Module 5 (12 MP, Raspberry Pi Ltd., UK), ESP8266 Wi-Fi module (Ai-Thinker Technology Co., Ltd, China) and embedded

computing unit. This unit processes the captured images using an improved YOLOv8 model and soft NMS method, thereby transferring the operation situation to Arduino Uno through USB 2.0 connection during processing and upload the processed image and calculating to GUI on mobile device with ESP8266 Wi-Fi module, which is depicted in Fig. 4 (b).

2.3. Real-time detection model of magnetic-bead-attached CTCs

2.3.1. Dataset preparation

In this study, the proposed CTCs analysis method requires robust object detection in dynamic fluid environments. Therefore, an improved YOLOv8 model was utilized for the development of two models for automatic bead-cell interaction analysis, which included cell-binding bead detection model and lung cancer cell detection model. To develop the improved YOLOv8 model, this study established two datasets for training and evaluation; the overall dataset preparation process workflow is depicted in Fig. 5. Initially, during data collection, 249 images were captured from the microfluidic-chip-based dynamic fluid platform. Subsequently, the data was cleaned to remove near-duplicate and blurry images through manual data screening; after cleaning, a total of 234 images remained. Each image, measuring 2430 x 1260 pixels, was divided into 16 sub-images of 340 x 160 pixels, allowing for smaller region analysis by the YOLO model and further improving detection and differentiation between minute entities. After partitioning, a total of 3,754 sub-images were used for subsequent analysis. To enhance the robustness of the model and reduce the risk of overfitting, we applied data augmentation to expand the dataset. The data augmentation strategy included six transformations: flipping, rotation, noise injection, cutout, cropping, and shearing [26–30]; each image was augmented with three random transformations. After applying these augmentation methods, the dataset was expanded to 11,262 images. The total data was divided into two types of datasets according to two annotation rules. In the first dataset, we focused on annotating magnetic beads in two categories: those attaching to cells and those not attaching; in the second dataset, we focused on annotating cells in two categories: lung cancer cells and non-lung cancer cells. For all annotations, this study utilized LabelImg software and saved the files in YOLO format. All annotations were processed by clinical professionals. After annotation, both datasets contained 11,262 images each, which were split into 7,884 images for training, 2,252 images for validation, and 1,126 images for testing.

The overall workflow for preparing a custom dataset and training the improved YOLOv8 model involves collecting images from a microfluidic

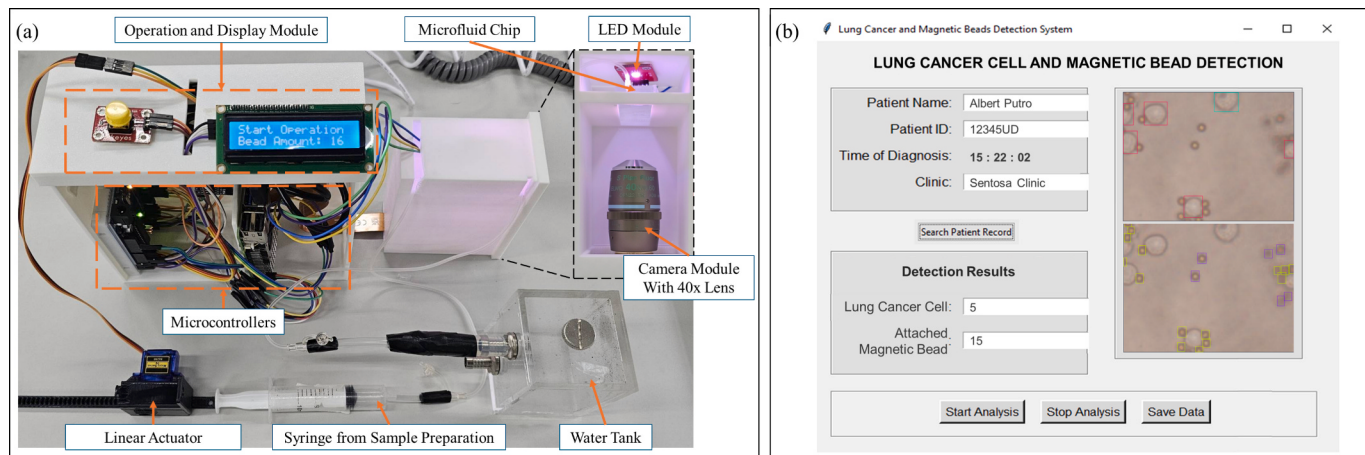


Fig. 4. (a) The hardware configuration of the portable device is divided into three parts: electrical, fluidic, and optical components. The electrical components include a button, an LCD display module, two microcontrollers, and a servo motor-driven linear actuator. The fluidic components consist of a syringe, a SMAC-structured microfluidic chip, and a water tank. The optical components comprise an LED module and a camera module with a 40x lens. (b) The GUI displays the patient's personal information, calculation results, and processed images.

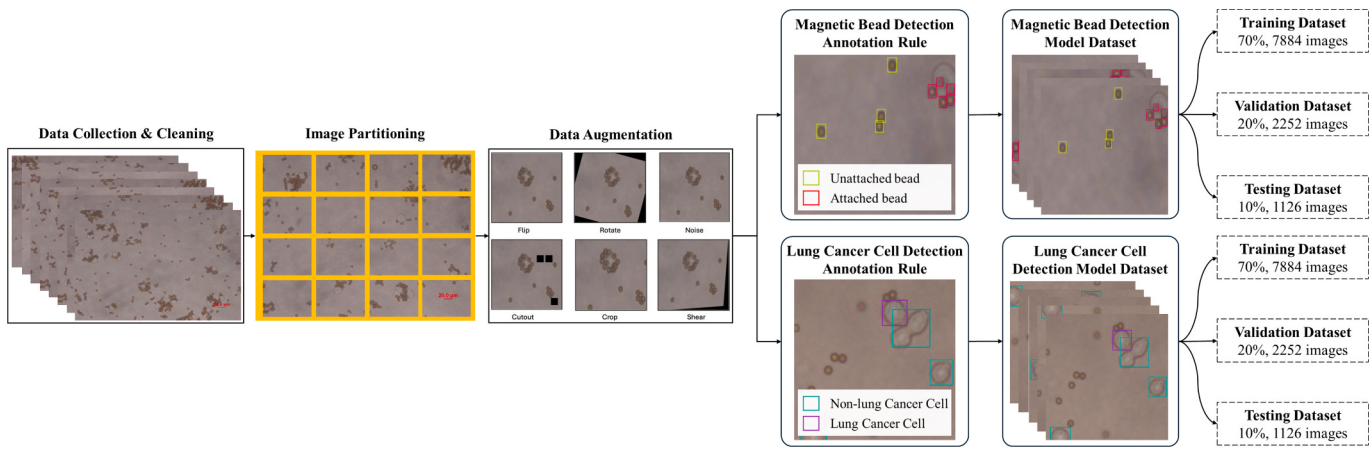


Fig. 5. The overall workflow for preparing custom datasets begins with the collection of 234 images, which are then partitioned into 3,754 sub-images and augmented to a total of 11,262 images. Two distinct datasets are annotated based on specific rules and subsequently split into training, validation, and testing datasets.

platform, cleaning and partitioning them into sub-images, applying data augmentation techniques to expand the dataset, annotating the images for specific object categories, and finally splitting the dataset into training, validation, and testing sets to effectively train the model for bead-cell interaction analysis.

2.3.2. Improved YOLOv8 model

The YOLOv8 model introduces significant advancements in object detection, offering both enhanced speed and accuracy through convolutional layers with residual connections [31–33], which are crucial for detecting complex structures such as cancer biomarkers. The model's neck, incorporating Feature Pyramid Networks (FPN) or Path Aggregation Networks (PAN), enhances multi-scale feature fusion, improving the detection of objects at various sizes. In this study, we modified the YOLOv8 architecture by integrating SE blocks and a GAM into the model's neck. These enhancements recalibrated the features and optimized attention, improving the detection accuracy of small and dense objects, such as magnetic beads attached to A549 lung cancer cells, enabling more precise magnetic bead and cancer cell detection in microfluidic images; the architectural modification of YOLOv8 model's neck is depicted in Fig. 6.

The SE block enhances the significance of individual channels in feature maps, improving the model's capacity for detailed image analysis. It operates in two phases, squeeze and excitation. In the squeeze

phase, spatial dimensions are reduced to a global context vector through global average pooling, capturing essential channel-wise information [34]:

$$z_c = \frac{1}{H \times W} \sum_{i=1}^H \sum_{j=1}^W u_c(i,j) \quad (1)$$

where $u_c(i,j)$ represents the activation at spatial location (i,j) in channel c , and H, W denote the spatial dimensions of the feature map. This operation captures essential channel-level statistics necessary for modeling contextual dependencies. Subsequently, during the excitation phase, the aggregated descriptor z is processed through a bottleneck structure consisting of two fully connected layers interleaved with a ReLU activation, followed by a sigmoid function to generate channel-wise modulation weights [34]:

$$s_c = \sigma(w_2 \delta(w_1 z_c)) \quad (2)$$

where δ denotes the ReLU activation, σ is the sigmoid activation function, W_1 and W_2 are the corresponding learnable weight matrices. Finally, the recalibrated weights s_c are applied to the original feature map through channel-wise multiplication, yielding the refined feature map \tilde{x}_c [34]:

$$\tilde{x}_c = u_c \cdot s_c \quad (3)$$

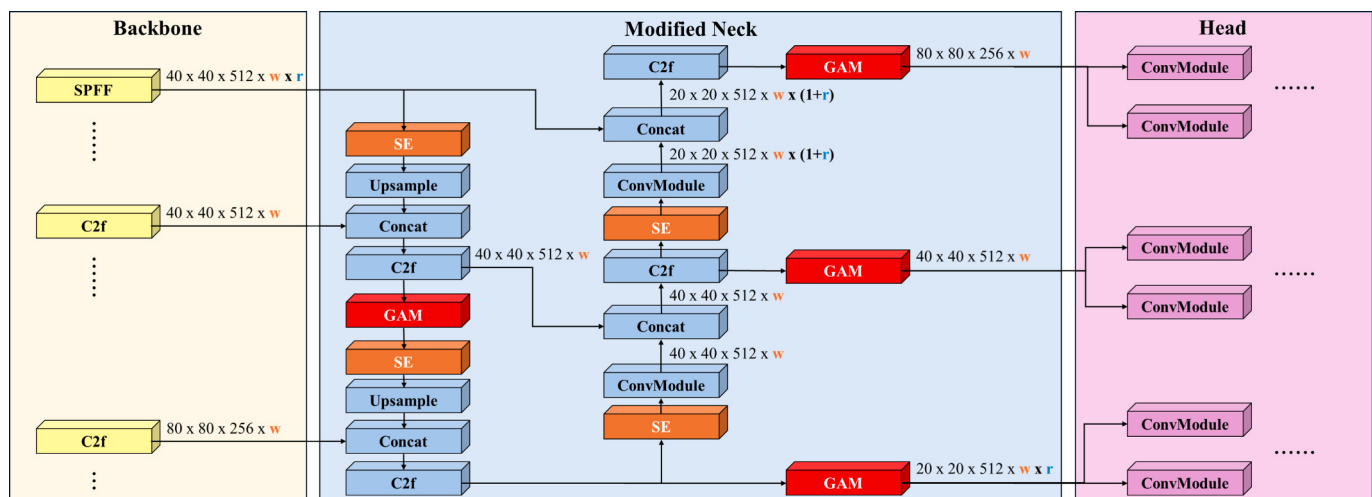


Fig. 6. Architectural modification of YOLOv8 model's neck.

The GAM improves feature representation by focusing on both channel and spatial dimensions, which is inspired by the Convolutional Block Attention Module (CBAM). The adapted GAM incorporates shortcut connections, ensuring efficient information flow and preventing degradation, described by [35]:

$$F_{output} = F_{input} + [M_S(M_C(F_{input}) \otimes F_{input}) \otimes (M_C(F_{input}) \otimes F_{input})] \quad (4)$$

Here, F_{input} is the input feature map processed by the GAM, and F_{output} is the output after passing through the attention mechanisms. The model combines channel attention M_C and spatial attention M_S , using element-wise multiplication \otimes to refine features. A residual connection is added to preserve the original information and prevent the loss of key features.

2.3.3. Post-processing techniques (NMS and Soft NMS)

Post-processing Techniques such as NMS and Soft NMS play a critical role in refining detections in the deep learning pipeline, particularly for magnetic bead and cancer cell detection. NMS eliminates redundant bounding boxes by retaining the one with the highest confidence score and discarding overlapping ones based on an intersection-over-union (IoU) threshold. This process is represented as [36]:

$$B_{final} = \max(B_i), i \in S \quad (5)$$

where B_{final} is the selected bounding box, B_i are the candidate boxes, and S is the set of all boxes exceeding the IoU threshold.

To address the limitations of traditional NMS in densely packed regions, we implemented Soft NMS, which reduces the scores of overlapping boxes proportionally to their IoU values rather than removing them entirely [36]:

$$s_i = s_i \times (1 - IoU(B, B_i)) \quad (6)$$

where s_i and B_i represents the score and bounding box of each overlapping detection, respectively. This approach allows for better detection in cases where objects (such as magnetic beads or cancer cells) are closely situated, preserving valuable detections, and improving the overall precision. By integrating both NMS and Soft NMS, the model enhances its ability to distinguish and quantify intricate biological structures, which is critical for effective cancer detection and magnetic bead analysis.

3. Experimental results

3.1. Performance of YOLOv8 model with different architectural modification and post-processing

In this experiment, we evaluated the performance of various configurations of YOLOv8 model, focusing on the interaction between Precision, Recall, and mAP across different architectural modifications and post-processing techniques. The analysis revealed significant variances in object detection and classification efficacy, described in Table 1. The baseline model (YOLOv8) with conventional Non-Maximum Suppression recorded a Precision of 0.924 and a Recall of 0.916. Transitioning to Soft NMS, there were improvements in the model, raising Precision to 0.926 and Recall to 0.918, enhancing mAP slightly to 0.943 (mAP 0.5) and 0.732 (mAP 0.5-0.95).

To validate the statistical significance of the performance improvements observed in the YOLOv8 model with SE & GAM, we conducted an independent *t*-test between the baseline YOLOv8 and YOLOv8 with SE & GAM. The results of this statistical analysis are presented in Table 2, which shows the *t*-statistic and *p*-value for each metric in both detection tasks (Magnetic Bead Detection and Lung Cancer Cell Detection).

The integration of the SE and GAM block into the model framework showed a nuanced impact on performance metrics. With NMS, the SE-powered model maintained a high mAP@0.5–0.95 of 0.745, and with Soft NMS, Precision slightly improved to 0.852. Introducing GAM with NMS pushed Precision to 0.936, demonstrating the mechanism's ability to refine the model's responsiveness to spatial nuances. Employing Soft NMS with these enhancements consistently uplifted performance, setting new benchmarks in Precision at 0.941 and mAP@0.5–0.95 at 0.748, as the dual enhancements of SE and GAM worked synergistically to optimize detection accuracy. The *t*-test results confirmed the statistical significance of these improvements, with *t*-values of -14.50 for mAP 0.5 and -12.30 for mAP 0.5-0.95, and *p*-values < 0.0001, indicating highly significant enhancements over the baseline model. Fig. 7 showcased the performance of magnetic bead detection model.

Similar outcomes were observed in the lung cancer cell detection model as illustrated in Fig. 8, also detailed in Table 1. The baseline model with NMS showed a respectable Precision of 0.833 and a Recall of 0.823. Switching to Soft NMS slightly boosted these metrics to 0.834 and 0.825, respectively, and maintained mAP scores. The integration of SE and GAM into the baseline model and applying Soft-NMS significantly improved the detection metrics, with Precision rising to 0.862 and Recall to 0.845, emphasizing the effectiveness of these advanced architectural features and post-processing techniques in enhancing model precision and recall. The *t*-test results further validated these improvements, with significant *t*-values (e.g., -13.20 for mAP 0.5) and

Table 1
Performance of different architectural modifications and post-processing based on YOLOv8 model on train 1–5.

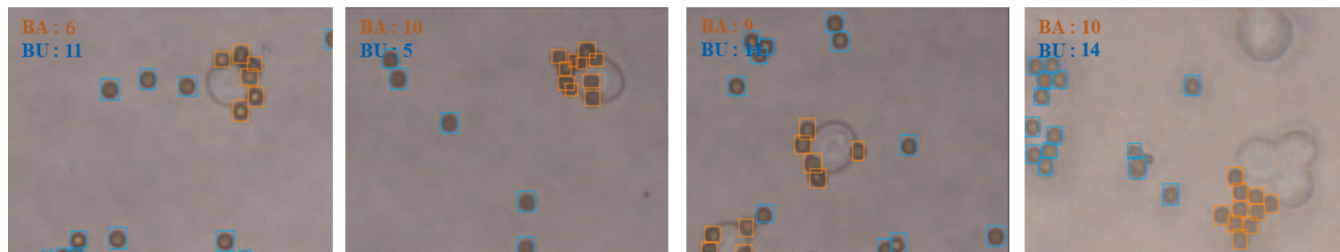
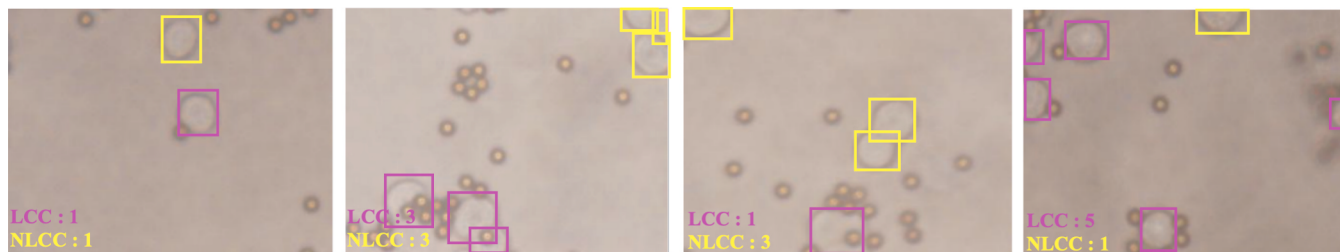
Model	Post-Processing	Magnetic Bead Detection				Lung Cancer Cell Detection			
YOLOv8	NMS	0.924 ± 0.012	0.916 ± 0.018	0.943 ± 0.009	0.731 ± 0.014	0.833 ± 0.016	0.823 ± 0.011	0.840 ± 0.007	0.636 ± 0.019
	Soft NMS	0.926 ± 0.015	0.918 ± 0.013	0.943 ± 0.011	0.732 ± 0.017	0.834 ± 0.012	0.825 ± 0.014	0.840 ± 0.008	0.638 ± 0.020
	NMS	0.931 ± 0.010	0.924 ± 0.016	0.953 ± 0.006	0.745 ± 0.012	0.852 ± 0.015	0.837 ± 0.009	0.858 ± 0.005	0.652 ± 0.018
	Soft NMS	0.932 ± 0.013	0.924 ± 0.014	0.955 ± 0.008	0.745 ± 0.015	0.852 ± 0.011	0.838 ± 0.012	0.859 ± 0.006	0.653 ± 0.017
YOLOv8 with SE	NMS	0.936 ± 0.009	0.923 ± 0.017	0.957 ± 0.007	0.746 ± 0.013	0.852 ± 0.014	0.841 ± 0.010	0.870 ± 0.004	0.679 ± 0.016
	Soft NMS	0.937 ± 0.011	0.924 ± 0.015	0.958 ± 0.009	0.748* ± 0.016	0.854 ± 0.013	0.841 ± 0.011	0.871 ± 0.005	0.679 ± 0.019
	NMS	0.938 ± 0.008	0.925* ± 0.012	0.968* ± 0.005	0.747 ± 0.011	0.861 ± 0.010	0.843 ± 0.008	0.883* ± 0.003	0.686 ± 0.015
YOLOv8 with SE & GAM	Soft NMS	0.941* ± 0.007	0.925* ± 0.006	0.968* ± 0.004	0.748* ± 0.012	0.862* ± 0.008	0.845* ± 0.007	0.883* ± 0.003	0.687* ± 0.010

* Denotes significant improvement

Table 2

T-test results of comparison between YOLOv8 and YOLOv8 with SE & GAM.

Post-Processing		Magnetic Bead Detection			Lung Cancer Cell Detection			
	Precision	Recall	mAP 0.5	mAP 0.5-0.95	Precision	Recall	mAP 0.5	mAP 0.5-0.95
t	Soft NMS	-6.70	-5.80	-14.50	-12.30	-5.90	-4.70	-13.20
p-value		*0.0002	*0.0005	*0.0001	*0.0001	*0.0004	*0.001	*0.0001

* Denotes differences significant ($p < 0.05$).**Fig. 7.** Performance of the proposed model in predicting bead attachment on cells. Blue boxes indicate beads unattached (BU) to cells, while orange boxes indicate beads attached (BA) to cells. (For interpretation of the references to colour in this figure legend, the reader is referred to the web version of this article.)**Fig. 8.** Performance of the proposed model in predicting lung cancer cells. Purple boxes indicate lung cancer cells (LCC), while yellow boxes indicate non-lung cancer cells (NLCC). (For interpretation of the references to colour in this figure legend, the reader is referred to the web version of this article.)

p -values < 0.0001 , confirming the statistical significance of the enhancements.

3.2. Comparative model analysis

Based on the result of section 3.1, we concluded that the YOLOv8 with SE and GAM block, incorporated with soft NMS post-processing method, was able to achieve best performance in all evaluation standards. Utilizing this processing method, this study compared the performance of different models, including YOLOv5, YOLOv8, SSD, and Faster R-CNN, which shared the same architectural modifications and post-processing methods within this experiment. These models were selected as references because they represent diverse deep learning object detection architectures relevant to biomedical imaging and real-time applications. Specifically, YOLOv5 is known for its high-speed single-stage detection capabilities; YOLOv8 served as a benchmark for evaluating the effectiveness of our modifications; SSD offers a different feature extraction mechanism, providing insights into performance

trade-offs among single-stage detectors; and Faster R-CNN is a two-stage model recognized for its high accuracy, albeit with greater computational demands. All models were evaluated on two tasks: magnetic bead detection and lung cancer cell detection. The comparative analysis, as revealed in Table 3, delineates a narrative of progressive refinement in object detection capabilities across the models tested. Starting with SSD, which established an initial benchmark with a Precision of 0.763 and Recall of 0.791 in magnetic bead detection; a Precision of 0.683 and Recall of 0.721 in lung cancer cell detection. Advancements were evident with Faster R-CNN, which improved Precision to 0.806 and Recall to 0.815 in magnetic bead detection; Precision to 0.725 and Recall to 0.734 in lung cancer cell detection. YOLOv5 further propelled the performance metrics, demonstrating a Precision of 0.913 and Recall of 0.922 in magnetic bead detection; a Precision of 0.833 and Recall of 0.840 in lung cancer cell detection, underscoring significant enhancements over its predecessors.

The pinnacle of this evolutionary trajectory was marked by YOLOv8. In magnetic bead detection, it achieved the highest Precision of 0.941

Table 3

Comparative evaluation between different object detection models on train 1–5.

Model with SE and GAM	Post-Processing	Magnetic Bead Detection			Lung Cancer Cell Detection				
		Precision	Recall	mAP 0.5	mAP 0.5-0.95	Precision	Recall	mAP 0.5	mAP 0.5-0.95
SSD	Soft NMS	0.763 ± 0.28	0.791 ± 0.25	0.810 ± 0.22	0.635 ± 0.32	0.683 ± 0.27	0.721 ± 0.24	0.723 ± 0.23	0.575 ± 0.30
Faster R-CNN		0.806 ± 0.25	0.815 ± 0.23	0.843 ± 0.21	0.682 ± 0.29	0.725 ± 0.26	0.734 ± 0.22	0.756 ± 0.24	0.635 ± 0.28
YOLOv5		0.913 ± 0.22	0.922 ± 0.21	0.954 ± 0.23	0.733 ± 0.27	0.833 ± 0.25	0.840 ± 0.26	0.871 ± 0.22	0.675 ± 0.29
YOLOv8		0.941* ± 0.21	0.925* ± 0.22	0.968* ± 0.24	0.748* ± 0.25	0.862* ± 0.23	0.845* ± 0.21	0.883* ± 0.26	0.687* ± 0.27

* Denotes significant improvement.

and Recall of 0.925, along with the most impressive mAP scores of 0.968 at IoU = 0.5 and 0.748 at IoU range 0.5 to 0.95. In lung cancer cell detection, it also achieved the highest Precision of 0.862 and Recall of 0.845, along with the most impressive mAP scores of 0.883 at IoU = 0.5 and 0.687 at IoU range 0.5 to 0.95. This analysis demonstrates the improved precision of the latest YOLO iteration in detecting magnetic beads and lung cancer cells, showcasing the significant advancements in object detection technology. The *t*-test results in Table 4 further confirm the superiority of YOLOv8 with SE & GAM, with highly significant *t*-values (e.g., -52.9150 for mAP 0.5) and *p*-values < 0.0001, indicating statistically significant improvements over Faster R-CNN. It emphasizes the significant strides made towards developing more accurate and reliable deep learning-based diagnostic tools.

3.3. Performance of embedded computing on raspberry Pi 5

To assess the performance of the improved YOLOv8 model with soft NMS embedded in the proposed portable device, this study conducted an experiment to compare the performance between a specific desktop equipped with a GPU NVIDIA GTX 1650, Raspberry Pi 5 integrated in proposed portable device and a specific desktop without GPU. Raspberry Pi 5 utilized a quad-core ARM Cortex-A76 CPU running at 2.4 GHz, while the specific desktop was equipped with Intel Core i5-10400 which is comparable x86 architecture CPU. In the experiment, the preparation steps for the samples can be referred to in Section 2.1, and liquid biopsy samples were acquired from patients participating in an IRB-approved clinical trial at Changhua Christian Hospital. Additionally, all images were captured from the Raspberry Pi Camera Module integrated into the portable device. Regarding the evaluation method, post-deployment accuracy was measured by comparing the model's predictions with ground truth labels.

Table 5 below illustrates comparison results of the experiment, differences in performance between the desktop with GPU, Raspberry Pi 5 and the desktop without GPU. Compared to desktop with GPU, Raspberry Pi 5 resulted in lower frames per second (FPS), which decreased from 20 FPS to 15 FPS. Conversely, when compared to desktop without GPU, Raspberry Pi 5 achieved higher FPS, improving from 11 FPS to 15 FPS. To conclude the performance of improved YOLOv8 model with soft NMS embedded in Raspberry Pi 5, although it was unable to achieve the high performance of desktop with GPU, the average inference time of Raspberry Pi 5 had reduced to lower than 0.15 s, which can assist in increasing the overall workflow efficiency of early-stage lung cancer detection.

3.4. Counting accuracy evaluation of proposed portable device under dynamic fluid environment

To evaluate the performance of the portable device under dynamic fluid environment, this study conducted the experiment of evaluating the counting accuracy of attached magnetic bead and lung cancer cell in the 1 min of syringe injection with flow rate 10 $\mu\text{L}/\text{min}$. In every 10 s, the proposed device recorded the counting result of attached magnetic bead and lung cancer cell; for the ground truth, the attendants were requested to count attached magnetic bead and lung cancer cell in 6 images, which are the raw images stored in every 10 s. In Fig. 9(a), the attendant utilized GUI on mobile device to record the ground truth; there were three attendants in this experiment. The counting accuracy is

Table 5

Performance comparison between different computing resource.

Model	Post-Processing	Computing Resource	FPS	Average Inference Time (s)
YOLOv8 with SE and GAM	Soft NMS	Intel Core i5-10400 & NVIDIA GTX 1650	20*	0.045*
		Raspberry Pi 5	15	0.121
		Intel Core i5-10400	11	0.153

* Denotes significant improvement.

calculated as:

$$\text{countingaccuracy} = \frac{N_D}{N_E} * 100\% \quad (6)$$

where N_D is the amount recorded by the portable device and N_E is the respective amount from ground truth. This experiment was repeated 15 times for each attendant.

In this experiment, we compared the counting accuracy between YOLOv8 and improved YOLOv8 with soft NMS, which were both trained with datasets defined in section 3.1 and embedded in Raspberry Pi 5 which integrated in portable device. From the counting accuracy result depicted in Fig. 9(b), we can observe that improved YOLOv8 with soft NMS has improved the average counting accuracy from 88.75 % to 96.96 % in attached magnetic bead, and from 87.36 % to 93.52 % in the lung cancer cell. As a result, the proposed portable device embedded with improved YOLOv8 incorporated soft NMS achieved higher counting accuracy under dynamic fluid environment than the YOLOv8.

4. Discussion

In order to address the challenge of improving the object detection accuracy of magnetic-bead-attached CTCs in dynamic environments, this study first developed an improved YOLOv8 model for the real-time detection of multiple target CTCs. This model was trained and evaluated on a microfluidic chip-based dynamic platform developed in previous studies. The ability of the proposed model and portable device to maintain high accuracy under dynamic fluid conditions underscores its potential for real-world clinical applications, where continuous blood flow and cell movement present significant challenges for CTC detection. The evaluation results demonstrated robust accuracy compared to the fundamental YOLOv8 model, with an actual counting accuracy of CTCs reaching 93.52 %. The *t*-test results further confirmed the statistical significance of these improvements, with highly significant *t*-values and *p*-values < 0.0001, indicating that the enhancements are not due to random chance but are a direct result of the SE and GAM modifications. After establishing the improved YOLOv8 model, this study also integrated a semi-automatic microfluidic chip-based dynamic platform and an IFC with an embedded computing unit for the improved YOLOv8 model, thereby developing a portable device to enhance the implementation of POCT in early-stage lung cancer diagnosis. In terms of real-time performance, the portable device equipped with a Raspberry Pi 5 achieved an FPS of 15, which is within the acceptable range of 15–20 FPS required for clinical applications involving dynamic fluid analysis [37]. This performance ensures accurate and continuous monitoring of

Table 4

T-test results of comparison between faster R-CNN and YOLOv8 with SE & GAM.

	Post-Processing	Magnetic Bead Detection			Lung Cancer Cell Detection			<i>t</i>	<i>p</i> -value
		Precision	Recall	mAP 0.5	mAP 0.5-0.95	Precision	Recall	mAP 0.5	mAP 0.5-0.95
Soft NMS		-36.3271 *0.0001	-28.5000 *0.0001	-52.9150 *0.0001	-45.0000 *0.0001	-32.0000 *0.0001	-22.0000 *0.0001	-48.0000 *0.0001	-40.0000 *0.0001

* Denotes differences significant (*p* < 0.05).

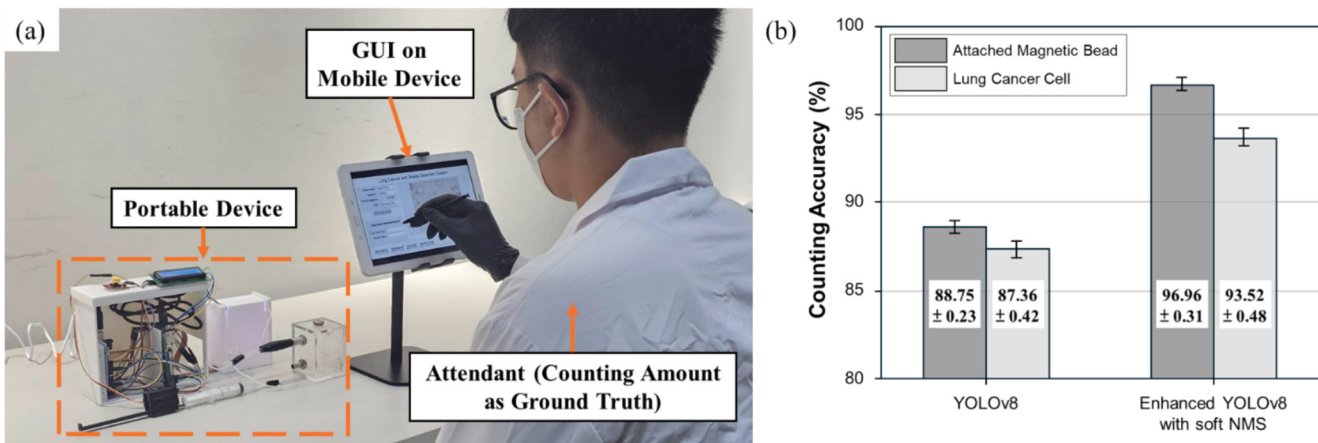


Fig. 9. (a) Experiment setup for amount ground truth collection. (b) Counting accuracy result of attached magnetic bead and lung cancer cell.

CTCs in real-time, making the device suitable for POCT scenarios. While the FPS is lower than the 20 FPS achieved by a desktop with a dedicated GPU, it significantly outperforms the 11 FPS of a desktop without a GPU, demonstrating the feasibility of using cost-effective, portable hardware for clinical diagnostics. The experimental results confirm that the proposed detection model of magnetic-bead-attached CTCs integrated into the portable device, consistently achieved high accuracy in dynamic fluid environments, enhancing its practicality for clinical applications. However, the use of A549 cells to simulate CTCs limits the applicability of the evaluation to actual clinical CTCs. While A549 cells are widely used as a model for lung cancer studies, it is important to note that the expression level of EpCAM in A549 cells cultured *in vitro* may differ from that of real CTCs derived from patient samples. According to previous studies [38,39], A549 cells exhibit moderate to high EpCAM expression, which is suitable for magnetic bead capture. However, real CTCs may show heterogeneous EpCAM expression due to tumor heterogeneity, which could affect capture efficiency. To improve the detection of patient-derived CTCs, the proposed microfluidic platform will undergo two key enhancements. First, to address the potential variability in EpCAM expression, we will validate the EpCAM levels in clinical CTCs obtained from patient samples and optimize the magnetic bead functionalization process to ensure robust capture efficiency across diverse CTC populations. Second, capitalizing on the high CTCs burden in small cell lung cancer (SCLC), a disease often diagnosed with widespread dissemination and a poor prognosis, we will obtain IRB-approved blood samples from SCLC patients. These samples are expected to provide a rich source of authentic clinical CTCs. We will process these samples using functionalized magnetic beads and then acquire images of the clinical CTCs, non-lung cancer cells, and attached/unattached beads. After manual screening by experts to remove low-quality images (duplicates and blurry images), the resulting clinical images will be integrated into the testing datasets, which is mentioned in section 2.3.1, “Dataset Preparation”. This clinical data-enhanced dataset will then be used to train and evaluate the improved YOLOv8 model, which should improve detection accuracy in clinical settings, increasing the platform’s clinical practicality and robustness. Finally, we will evaluate the detection performance of clinical CTCs under dynamic fluid conditions by comparing the counts generated by our portable device to those obtained by clinical professionals. This evaluation will mirror the methodology detailed in section 3.4, “Counting Accuracy Evaluation of Proposed Portable Device Under Dynamic Fluid Environment.” While these results reflect promising progress toward a deployable point-of-care system, it is important to acknowledge that the current implementation still has technical limitations that must be addressed. These include manual preprocessing, potential instability under uncontrolled environments, and reliance on model CTCs. These challenges are summarized in Section 5, which outlines the key technical barriers

remaining before full clinical translation.

5. Limitation

Despite the promising results demonstrated in this study, several limitations should be acknowledged to provide a more realistic assessment of the current system’s readiness for clinical deployment.

(1). Although A549 cell lines are widely used as surrogates for lung cancer CTCs, they may not accurately reflect the biological heterogeneity of actual patient-derived CTCs. Variability in EpCAM expression among clinical samples can impact magnetic bead binding efficiency and detection rates. To address this, future studies will include validation using patient-derived CTCs with varying EpCAM expression levels.

(2). While red blood cell lysis and density gradient centrifugation were applied to improve input quality, these steps were carried out manually using benchtop procedures. Although recent studies have shown the feasibility of integrating such preprocessing into microfluidic chips [40,41], the miniaturization and automation of these modules remain a challenge. In particular, maintaining consistency across different blood samples and ensuring effective on-chip separation within limited device space require further engineering optimization.

(3). The current system’s performance, including high-resolution images and stable detection, was achieved under well-controlled laboratory settings using a bench microscope and fixed lighting conditions. In real POCT environments, factors such as vibration, ambient lighting, and temperature fluctuations may degrade image quality and detection accuracy. In our own experiments, we encountered considerable difficulty in maintaining consistent image clarity and had to repeat image acquisition several times before obtaining usable data. This highlights the need for further development in illumination control and system stabilization.

These limitations reflect ongoing technical hurdles that must be overcome before the system can be deployed in fully autonomous POCT applications. Future work will focus on refining the preprocessing workflow, improving robustness under variable imaging conditions, and validating the system with clinical CTC samples.

6. Conclusion

In this study, an improved magnetic bead dynamic analysis method was proposed to automatically and precisely count the amount of attached magnetic beads under dynamic fluid environment, assisting in reducing labor-intensive tasks of magnetic bead-based CTCs analysis. Moreover, this study integrated the components of microfluidic-chip-based dynamic fluid platform and embedded computing unit for dynamic magnetic bead analysis method. The application of this study can not only increase the automatic detection robustness and portability of

dynamic magnetic bead-based CTCs analysis but also improve the POCT implementation for early-stage lung cancer detection.

CRediT authorship contribution statement

Asydickey Firmanto: Writing – review & editing, Writing – original draft, Conceptualization. **Tsung-Wei Lin:** Writing – original draft, Validation, Software, Data curation, Conceptualization. **Yi-Chun Du:** Writing – review & editing, Writing – original draft, Visualization, Validation, Supervision, Project administration, Methodology, Investigation, Funding acquisition, Formal analysis. **Chun-Ping Jen:** Visualization, Validation, Supervision, Project administration, Investigation, Funding acquisition.

Declaration of competing interest

The authors declare that they have no known competing financial interests or personal relationships that could have appeared to influence the work reported in this paper.

Acknowledgments

This work was supported in part by the National Science and Technology Council, Taiwan, under Grant 113-2622-E-006-026 and 111-2221-E-006-032-MY3.

Data availability

The data that has been used is confidential.

References

- [1] A.A. Thai, B.J. Solomon, L.V. Sequist, J.F. Gainor, R.S. Heist, Lung cancer, *Lancet* 398 (10299) (Aug. 2021) 535–554, [https://doi.org/10.1016/S0140-6736\(21\)00312-3](https://doi.org/10.1016/S0140-6736(21)00312-3).
- [2] G. Boloker, C. Wang, J. Zhang, Updated statistics of lung and bronchus cancer in United States (2018), *J. Thorac. Dis.* 10 (3) (Mar. 2018) 1158–1161, <https://doi.org/10.21037/jtd.2018.03.15>.
- [3] A. Leiter, R.R. Veluswamy, J.P. Wisnivesky, The global burden of lung cancer: current status and future trends, *Nat. Rev. Clin. Oncol.* 20 (9) (Sep. 2023) 624–639, <https://doi.org/10.1038/s41571-023-00798-3>.
- [4] F. Bray, J. Ferlay, I. Soerjomataram, R.L. Siegel, L.A. Torre, A. Jemal, Global cancer statistics 2018: GLOBOCAN estimates of incidence and mortality worldwide for 36 cancers in 185 countries, *CA Cancer J. Clin.* 68 (6) (Nov. 2018) 394–424, <https://doi.org/10.3322/caac.21492>.
- [5] M.H. Al-Azri, Delay in cancer diagnosis: causes and possible solutions, *Oman Med. J.* 31 (5) (Sep. 2016) 325–326, <https://doi.org/10.5001/omj.2016.65>.
- [6] R. Nooreldien, H. Bach, Current and future development in lung cancer diagnosis, *Int. J. Mol. Sci.* 22 (16) (Aug. 2021) 8661, <https://doi.org/10.3390/ijms22168661>.
- [7] V. Iyer, Z. Yang, J. Ko, R. Weissleder, D. Issadore, Advancing microfluidic diagnostic chips into clinical use: a review of current challenges and opportunities, *Lab Chip* 22 (17) (2022) 3110–3121, <https://doi.org/10.1039/D2LC00024E>.
- [8] F.A. Ganchi, T.C. Hardcastle, Role of point-of-care diagnostics in lower- and middle-income countries and austere environments, *Diagnostics* 13 (11) (Jun. 2023) 1941, <https://doi.org/10.3390/diagnostics13111941>.
- [9] I. Heidrich, L. Aćkar, P. Mossahebi Mohammadi, and K. Pantel, “Liquid biopsies: Potential and challenges,” *Int J Cancer*, vol. 148, no. 3, pp. 528–545, Feb. 2021, doi: 10.1002/ijc.33217.
- [10] Y. Fu, Y. Zhang, B.L. Khoo, Liquid biopsy technologies for hematological diseases, *Med. Res. Rev.* 41 (1) (Jan. 2021) 246–274, <https://doi.org/10.1002/med.21731>.
- [11] J. Sierra, J. Marrugo-Ramírez, R. Rodriguez-Trujillo, M. Mir, J. Samitier, Sensor-integrated microfluidic approaches for liquid biopsies applications in early detection of cancer, *Sensors* 20 (5) (Feb. 2020) 1317, <https://doi.org/10.3390/s20051317>.
- [12] S. Togo, et al., Sensitive detection of viable circulating tumor cells using a novel conditionally telomerase-selective replicating adenovirus in non-small cell lung cancer patients, *Oncotarget* 8 (21) (May 2017) 34884–34895, <https://doi.org/10.18632/oncotarget.16818>.
- [13] Y. Li, et al., Clinical significance of circulating tumor cells and tumor markers in the diagnosis of lung cancer, *Cancer Med.* 8 (8) (Jul. 2019) 3782–3792, <https://doi.org/10.1002/cam4.2286>.
- [14] C. Poggiani, E. Rossi, R. Zamarchi, Possible role of circulating tumor cells in early detection of lung cancer, *J. Thorac. Dis.* 12 (7) (Jul. 2020) 3821–3835, <https://doi.org/10.21037/jtd.2020.02.24>.
- [15] C. Mayo, et al., CK-coated magnetic-based beads as a tool to isolate circulating tumor cells (CTCs) in human tumors, *Transl Lung Cancer Res.* (2013) 65–71.
- [16] Y. Gao, W.-H. Fan, Z. Song, H. Lou, X. Kang, Comparison of circulating tumor cell (CTC) detection rates with epithelial cell adhesion molecule (EpCAM) and cell surface vimentin (CSV) antibodies in different solid tumors: a retrospective study, *PeerJ* 9 (Mar. 2021) e10777, <https://doi.org/10.7717/peerj.10777>.
- [17] G.M. van de Geijn, M. van Gent, N. van Pul-Bom, M.H. Beunis, A.J.P. van Tilburg, T.L. Njo, A new flow cytometric method for differential cell counting in ascitic fluid, *Cytometry B Clin. Cytom.* 90 (6) (Nov. 2016) 506–511, <https://doi.org/10.1002/cyto.b.21171>.
- [18] W. Fan, D. Liu, W. Ren, C. Liu, Trends of bead counting-based technologies toward the detection of disease-related biomarkers, *Front. Chem.* 8 (Dec. 2020), <https://doi.org/10.3389/fchem.2020.600317>.
- [19] T.-C. Su, H. Vu-Dinh, S.-H. Lin, L. Do Quang, T. Chu Duc, and C.-P. Jen, “The effect of magnetic bead size on the isolation efficiency of lung cancer cells in a serpentine microchannel with added cavities,” *Biomed Microdevices*, vol. 26, no. 1, p. 7, Mar. 2024, doi: 10.1007/s10544-023-00689-5.
- [20] H. Vu-Dinh, et al., Immunomagnetic separation in a novel cavity-added serpentine microchannel structure for the selective isolation of lung adenocarcinoma cells, *Biomed. Microdevices* 23 (4) (Dec. 2021) 51, <https://doi.org/10.1007/s10544-021-00589-6>.
- [21] Y.J. Heo, D. Lee, J. Kang, K. Lee, W.K. Chung, Real-time image processing for microscopy-based label-free imaging flow cytometry in a microfluidic chip, *Sci. Rep.* 7 (1) (Sep. 2017) 11651, <https://doi.org/10.1038/s41598-017-11534-0>.
- [22] S. Zhou, B. Chen, E.S. Fu, H. Yan, Computer vision meets microfluidics: a label-free method for high-throughput cell analysis, *Microsyst. Nanoeng.* 9 (1) (Sep. 2023) 116, <https://doi.org/10.1038/s41378-023-00562-8>.
- [23] A.J. Ruiz-Rodríguez, et al., Deep phenotypic characterisation of CTCs by combination of microfluidic isolation (IsoFlux) and imaging flow cytometry (ImageStream), *Cancers (Basel)* 13 (24) (Dec. 2021) 6386, <https://doi.org/10.3390/cancers13246386>.
- [24] A. Muchlisńska, J. Smentoch, A.J. Żaczek, N. Bednarz-Knoll, Detection and characterization of circulating tumor cells using imaging flow cytometry—a perspective study, *Cancers (Basel)* 14 (17) (Aug. 2022) 4178, <https://doi.org/10.3390/cancers14174178>.
- [25] H.S. Park, N.H. Jeoung, Autocrine motility factor secreted by HeLa cells inhibits the growth of many cancer cells by regulating AKT/ERK signaling, *Biochem. Biophys. Res. Commun.* 525 (3) (May 2020) 557–562, <https://doi.org/10.1016/j.bbrc.2020.02.135>.
- [26] M. Cossio, “Augmenting Medical Imaging: A Comprehensive Catalogue of 65 Techniques for Enhanced Data Analysis,” Mar. 2023, [Online]. Available: <http://arxiv.org/abs/2303.01178>.
- [27] C. Shorten, T.M. Khoshgoftaar, A survey on image data augmentation for deep learning, *J. Big Data* 6 (1) (Dec. 2019) 60, <https://doi.org/10.1186/s40537-019-0197-0>.
- [28] C. Zhang, et al., A deep learning image data augmentation method for single tumor segmentation, *Front. Oncol.* 12 (Feb. 2022), <https://doi.org/10.3389/fonc.2022.782988>.
- [29] N. Moshkov, B. Mathe, A. Kertesz-Farkas, R. Hollandi, P. Horvath, Test-time augmentation for deep learning-based cell segmentation on microscopy images, *Sci. Rep.* 10 (1) (Mar. 2020) 5068, <https://doi.org/10.1038/s41598-020-61808-3>.
- [30] R. Hao, K. Namdar, L. Liu, M.A. Haider, F. Khalvati, A comprehensive study of data augmentation strategies for prostate cancer detection in diffusion-weighted MRI using convolutional neural networks, *J. Digit. Imaging* 34 (4) (Aug. 2021) 862–876, <https://doi.org/10.1007/s10278-021-00478-7>.
- [31] M. Hussain, YOLO-v1 to YOLO-v8, the Rise of YOLO and its complementary nature toward digital manufacturing and industrial defect detection, *Machines* 11 (7) (Jun. 2023) 677, <https://doi.org/10.3390/machines11070677>.
- [32] J. Terven and D. Cordova-Esparza, “A Comprehensive Review of YOLO: From YOLOv1 and Beyond,” Apr. 2023.
- [33] M. Lalinia, A. Sahafi, Colorectal polyp detection in colonoscopy images using YOLO-V8 network, *Signal Image Video Process* 18 (3) (Apr. 2024) 2047–2058, <https://doi.org/10.1007/s11760-023-02835-1>.
- [34] J. Hu, L. Shen, and G. Sun, “Squeeze-and-Excitation Networks,” in 2018 IEEE/CVF Conference on Computer Vision and Pattern Recognition, IEEE, Jun. 2018, pp. 7132–7141. doi: 10.1109/CVPR.2018.00745.
- [35] Yichao Liu, Zongru Shao, and Nico Hoffmann, “Global Attention Mechanism: Retain Information to Enhance Channel-Spatial Interactions,” Dec. 2021.
- [36] N. Bodla, B. Singh, R. Chellappa, and L. S. Davis, “Soft-NMS — Improving Object Detection with One Line of Code,” in 2017 IEEE International Conference on Computer Vision (ICCV), IEEE, Oct. 2017, pp. 5562–5570. doi: 10.1109/ICCV.2017.593.
- [37] S. Balter, Fluoroscopic frame rates: not only dose, *Am. J. Roentgenology* 203 (3) (Sep. 2014) W234–W236, <https://doi.org/10.2214/AJR.13.11041>.
- [38] M. Czaplicka, et al., Effect of varying expression of EpCAM on the efficiency of CTCs detection by SERS-based immunomagnetic optofluidic device, *Cancers (Basel)* 12 (11) (Nov. 2020) 3315, <https://doi.org/10.3390/cancers12113315>.
- [39] A. Coppolino, et al., Standard markers for detection of circulating tumor cells are variably expressed in pulmonary adenocarcinomas and are downregulated in cells undergoing mesenchymal transition, *J. Am. Coll. Surg.* 215 (3) (Sep. 2012) S40, <https://doi.org/10.1016/j.jamcollsurg.2012.06.122>.
- [40] M. Kim, S. Mo Jung, K. Lee, Y. Jun Kang, and S. Yang, “A Microfluidic Device for Continuous White Blood Cell Separation and Lysis From Whole Blood,” *Artif. Organs*, vol. 34, no. 11, pp. 996–1002, Nov. 2010, doi: 10.1111/j.1525-1594.2010.01114.x.
- [41] M. Toner, D. Irimia, Blood-on-a-chip, *Annu. Rev. Biomed. Eng.* 7 (1) (Aug. 2005) 77–103, <https://doi.org/10.1146/annurev.bioeng.7.011205.135108>.